Comparison of Candidate Designs and Performance Optimization for an Electric Traction Motor Targeting 50 kW/L Power Density

Nanjun Tang* and Ian P. Brown*
*Dept. of Electrical and Computer Engineering
Illinois Institute of Technology
Chicago, IL USA
ntang3@hawk.iit.edu and ibrown1@iit.edu

Abstract—The continued expansion of the global electric vehicle fleet is accompanied by an unprecedented demand for high power density electric traction motors. With the ambitious U.S. DRIVE 2025 target of 50 kW/L power density and an equally aggressive cost reduction goal, innovative approaches have to be utilized in terms of both the design and manufacturing of electric traction motors. In this paper, six motor options are compared and the best design is picked for each option to investigate the drive and excitation requirements and the weighted power efficiency over multiple load points, with necessary mechanical stress and demagnetization checks. State-of-the-art winding technologies, including high slot fill die compressed windings and hairpin windings, and rotors both with permanent magnet (PM) and PM-free are incorporated. The design of high flux density and low harmonic content magnetic field is also demonstrated.

Index Terms—electric traction motor, electric vehicle (EV), hairpin winding, high power density motor, optimization

I. INTRODUCTION

The U.S. DRIVE partnership has set the aggressive volumetric power density and cost targets of 50 kW/L and 3.3 \$/kW for 2025 100 kW electric vehicle (EV) traction motors [1]. An Electric Drives Technologies (EDT) Consortium of which the main focus is to meet the U.S. DRIVE 2025 targets has been funded by the U.S. Department of Energy.

Three electric motor types are currently used for production EVs—induction machines (e.g., Tesla Model S), wound field synchronous machines (e.g., Renault Zoe), and synchronous machines with interior permanent magnet (IPM) rotors (e.g., General Motors Chevy Bolt, Nissan Leaf, and Toyota Prius)—with the last being the most prevalent type. To achieve such a high power density as 50 kW/L, an electric motor needs to operate at elevated speeds and also with significantly increased torque density.

Higher rotor speeds are promoted with the development of high strength electrical steels, whereas increasing the torque production requires a higher current loading and airgap flux density. Feasible current loadings mainly depend on winding slot fills, AC loss mitigation techniques, and heat removal technologies. Hairpin windings are one example of high slot

Support provided by the USA Dept. of Energy EERE Program under award EE0008713.

fill windings that have found adoption in high performance EV traction motors [2], while die compressed windings [3] and cast windings [4] have the potential to push the slot fills even further. Standard cooling technologies such as spray cooling and jacket cooling may be enhanced, or new technologies such as integrated heat pipes can be utilized. Compared to the current loading, the airgap flux density is relatively confined since increases in soft magnetic material saturation flux densities are difficult and only limited improvements in hard permanent magnetic (PM) material remanence and coercivity are likely possible.

The purpose of this paper is to identify motor options, components, and required technologies that are likely to meet the U.S. DRIVE 2025 targets. In the subsequent sections, the sizing of the motor and the choice of the load points according to the EDT Consortium recommendations are first discussed. Then a reference motor is designed with a twolayer U-shape IPM rotor optimized for high flux density and low harmonic content to determine the required excitation and the proper thresholds for performance constraints. Next, six motor options, each featuring different combinations of die compressed winding, hairpin winding, wound field rotor, or IPM rotor, are investigated. For every option, the best design is selected from a collection of samples, with an emphasis of the weighted power efficiency. Other key performance metrics, including the current density and PM content, are also compared to locate the most promising candidates. Mechanical stress analysis and demagnetization checks are also discussed.

II. MOTOR SIZING AND LOAD POINTS FOR WEIGHTED EFFICIENCY ASSESSMENT

A. Choice of Major Dimensions

To meet the U.S. DRIVE 2025 traction motor targets of 100 kW peak power with a power density of 50 kW/L, the motor can have a volume of merely 2 L. Though it is not clearly defined in the U.S. DRIVE 2025 targets what components must be included in the volumetric power density evaluation, in this study, the end winding space has also been accounted for in the volume estimation. A stator outer diameter of 119.6 mm and a stack length of 143.5 mm are chosen to balance the

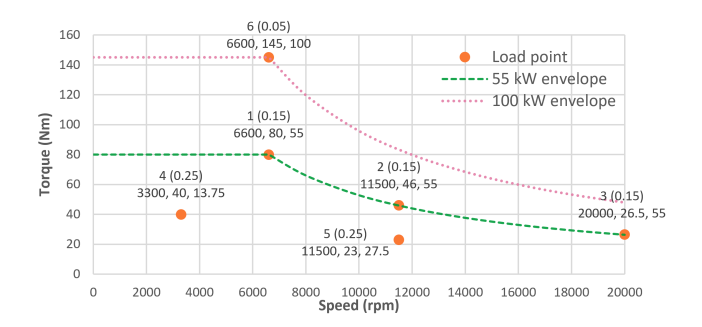


Fig. 1. Load points 1-6 for the weighted efficiency assessment, labeled as "No. (weight) rpm, Nm, kW."

active volume utilization and the axial cooling, which gives a 1.2 aspect ratio and a stack volume of 1.612 L. The stack volume, or the active volume, is 80.6% of the total volume allowed of 2 L.

B. Set of Load Points

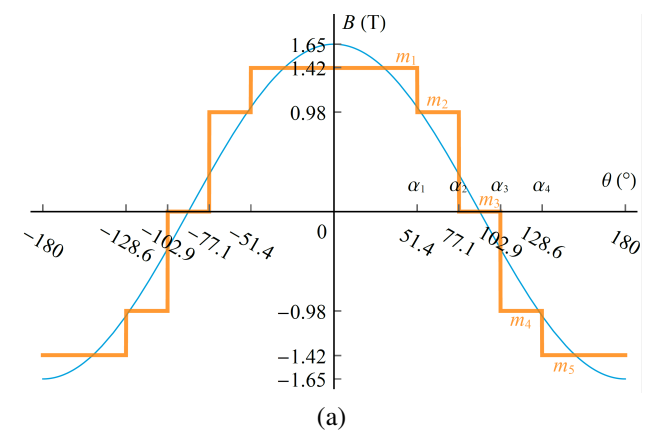
According to the recommendations by the motor technology focused members of the EDT Consortium [5], [6], the motor may not exceed the maximum speed of 20000 rpm and needs to achieve a constant power speed range ratio of no less than 3:1. A corner speed of 6600 rpm with a 20000 rpm maximum speed has been chosen and six load points are defined with the suggested ratios to the corner speed and weights to assess the overall motor efficiency, as shown in Fig. 1.

In particular, load points (LPs) 1–3 are on the 55 kW continuous power envelope, with LP1 being at the corner speed of 6600 rpm, LP3 at the maximum speed of 20000 rpm, and LP2 at the geometric mean of the two speeds aforementioned. LP4 is at half the corner speed and half the output torque of LP1. LP5 is at the same speed but half the torque of LP2. Finally, LP6 corresponds to the peak power output of 100 kW at the corner speed.

III. REFERENCE MOTOR DESIGN WITH A TWO-LAYER U-SHAPE IPM ROTOR

A reference motor is designed to assess the feasibility of the major dimensions previously selected and the excitation requirements to deliver all the load points in Fig. 1. The performance metrics of this reference design will also be used to determine the thresholds for optimization constraints such as current density, torque ripple, and kVA rating for other motor options. The reference design features a 12-slot 10-pole fractional-slot concentrated winding (FSCW) and a two-layer U-shape IPM rotor. For this application, the rotor needs to be designed for a high flux density with low harmonic content, hence the U-shape IPM rotor is selected for its magnet holding capacity and the harmonic control of the airgap magnetic field. The number of magnet layers has to be limited to two due to the small cross-section of the rotor. Otherwise the magnets will be too thin and difficult to handle in manufacturing.

Based on the underlying relationship among different harmonic orders [7], a two-layer IPM rotor can be designed to



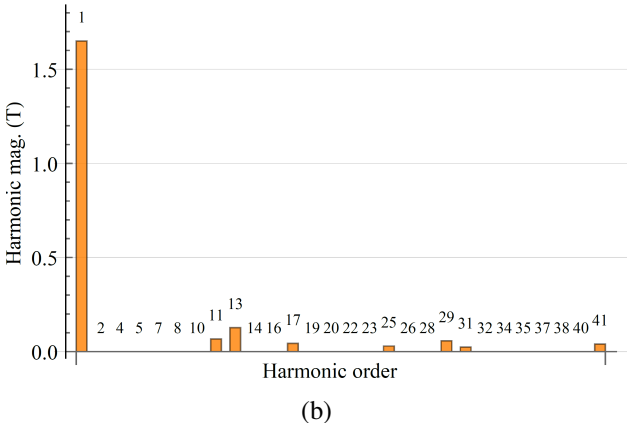


Fig. 2. Magnetic field design of the two-layer U-shape IPM rotor to produce high flux density with a low harmonic content: (a) airgap flux density distribution and its fundamental component and (b) harmonic content.

eliminate space harmonic orders of 5, 7, 19, 23, 35, 37, ... in the airgap flux density distribution, without introducing any even-order harmonics. Using the solution technique in [8], a high fundamental airgap flux density of 1.65 T with the desired low harmonic content is achieved by optimizing the parameters α_1 – α_4 and m_1 – m_5 , as shown in Fig. 2(a). The harmonic orders 5, 7, 19, 23, 35, 37, ... can be seen eliminated from the spectrum in Fig. 2(b). Then, the cross-section of a two-layer U-shape IPM rotor with 10 poles (or 5 pole pairs) is designed to realize the airgap magnetic field as shown in Fig. 2(a), based on the analytical modeling of the multilayer U-shape IPM rotor airgap magnetic field presented in [9].

A 12-slot stator is subsequently designed for this 10-pole rotor, as shown in Fig. 3. The stator winding is thus a 12-slot 10-pole FSCW, which has the potential for high slot fills. With conventional technologies, slot fills up to 55% are possible. By using a joint or segmented structure combined with pressing or compression, slot fills up to 75–78% are reported in the literature [10].

IV. CANDIDATE MOTOR OPTIONS AND DESIGN VARIABLES

To identify the motor options that have the best potential to meet the U.S. DRIVE 2025 50 kW/L power density target,

TABLE I SUMMARY OF CANDIDATE MOTOR OPTIONS

Option	U2a	U2b	V1	V2	FR	FH
Slot/pole	12/10	12/10	60/10	60/10	60/10	60/10
Stator winding-s.f.	FSCW-0.55	FSCW-0.65	Hairpin-0.63 ^a	Hairpin-0.63 ^a	Random-0.47	Hairpin-0.64 ^a
Rotor	IPM-U, 2-layer	IPM-U, 2-layer	IPM-V, 1-layer	IPM-V, 2-layer	WF, s.f. 0.72	WF, s.f. 0.72
Parameter categories	Airgap, stator					
Parameter count	6	6	13	22	12	12

^aVariable and design specific. Reported according to the selected design.

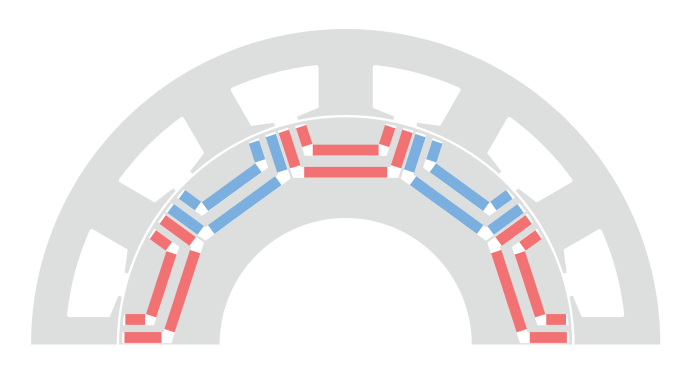


Fig. 3. Reference motor design with the two-layer U-shape IPM rotor.

various motor components—including FSCWs, hairpin windings, IPM rotors, and wound field rotors—and six different combinations thereof are considered. Each option is assigned a unique identifier as listed in Table I. The reference motor design which has a 12-slot 10-pole FSCW of 0.55 slot fill ("s.f.," defined as the ratio of net copper area and total slot area) belongs to option U2a and the variant of this option with a higher winding slot fill of 0.65 is designated U2b. The four remaining options are 60-slot 10-pole motors with either an IPM rotor (V1 and V2) or a wound field rotor (FR and FH).

Due to the limit pushing nature of the power density target, advanced winding technologies with higher slot fills have to be considered. For example, V1, V2, and FH feature hairpin windings that achieve 0.63–0.64 slot fills. The 0.65 slot fill of the stator winding of U2b and the field winding's 0.72 slot fill of FR and FH would require implementations as die compressed windings. In contrast, the lower slot fills of the U2a and FR stator windings are more representative of conventional technologies.

The major dimensions—stator outer diameter of 119.6 mm and the stack length of 143.5 mm—are the same across all options and kept constant. Each motor option also has a number of geometry related parameters to be optimized. The categories and counts of parameters are listed in Table I. Options V1, V2, FR, and FH have fully parameterized stator and rotor templates, resulting in more parameters. In contrast, options U2a and U2b assume the same fixed rotor design and have fewer parameters. The dimensional parameters for each stator or rotor template are per unitized to preclude infeasible geometries. However, the range of each parameter is still carefully tailored as not to be overly broad or narrow, which

can otherwise lead to unreasonable designs even without the detection of any geometry conflicts.

V. MOTOR PERFORMANCE CALCULATION AND DESIGN SAMPLING

A. Motor Performance Calculation Procedures

For every design, the preparation of geometry, the calculations in Motor-CAD, and the post-processing of the results are fully automated with a Python script dedicated to each motor option. For each load point, the excitation current magnitude and phase are first estimated with an analytical model and then verified with FEA simulation in every iteration. Up to six iterations will be performed for each load point to ensure to the torque output is within 100±0.5% of the defined amount while the voltage is not exceeding the limit determined by the DC bus voltage and the maximum modulation index (650 V and 0.94 for all motor options). It is likely that for some designs, only a partial amount of the required torque output can be delivered for certain load points (most often LP6) when also trying to stay within the voltage limit, in which case the calculation for that load point will terminate after six iterations and the maximum torque achievable is recorded.

B. Design Sampling, Objective, and Constraints

To find the best design, either a sweep ("sampling") of the parameter space or an optimization can be performed. Considering the number of design parameters and the time consumed to calculate each design, direct optimization is not a feasible approach in most cases. In this study, a collection of samples is generated with Advanced Latin Hypercube Sampling for each motor option. Then either the best design can be picked from the samples or based on the sampling data, metamodeling technique such as the Metamodel of Optimal Prognosis (MOP) [11] can be utilized for an MOP-based optimization [12], [13] to check if further improvements are found

The criteria for selecting the best design or setting up an optimization include the objective to maximize the weighted efficiency, and several constraints. The constraints that are common to all motor options are the maximum peak line-to-line voltage, the minimum per unit torque, the maximum torque ripple, and the maximum current densities, across all load points. In addition, options U2a, U2b, V1, and V2 have an input kVA constraint, whereas FR and FH have a field power loss constraint.

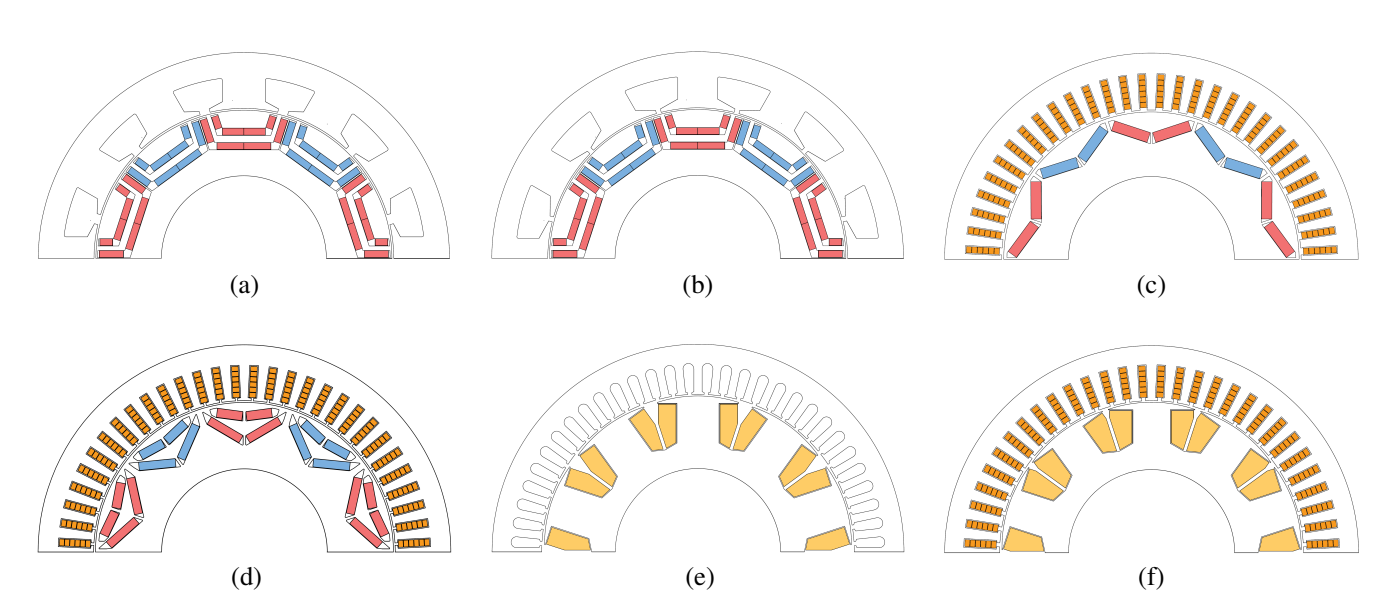


Fig. 4. Selected design for each motor option: (a) U2a, (b) U2b, (c) V1, (d) V2, (e) FR, and (f) FH.

TABLE II
SUMMARY OF THE SELECTED DESIGN FOR EACH MOTOR OPTION

Option	U2a	U2b	V1	V2	FR	FH
Total samples	16	105	214	500	113	145
Airgap (mm)	0.544	0.492	0.577	0.523	0.5	0.443
Split ratio	0.72 (fixed)	0.72 (fixed)	0.714	0.722	0.751	0.727
Weighted efficiency (%)	93.24	93.99	94.77	95.32	93.07	94.41
Stator current den. (A/mm ²), cont./peak	24/47.9	20/41	23.1/43.3	22.9/41.3	26.8/46	20.7/35.3
Rotor current den. (A/mm ²), cont./peak	N/A	N/A	N/A	N/A	24.4/40.4	21.9/35.2
Rotor PM volume (cm ³)	142.39	142.39	92.20	129.15	N/A	N/A

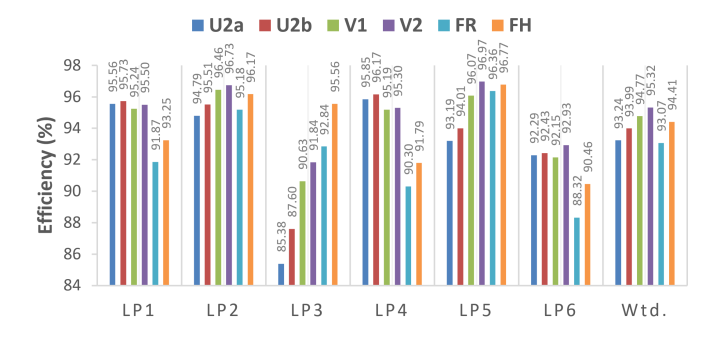


Fig. 5. Comparison of load point and the weighted efficiency of the selected designs for all six motor options.

VI. RESULTS

For each motor option, more than 100 samples are collected with the only exception of U2a, which is considered less promising than its higher slot fill counterpart, U2b. The best design selected from the samples for each option according to the aforementioned criteria is shown in Fig. 4. In particular, the picked design must be able to deliver the required torque for all load points within the voltage limit of the drive, while maximizing the weighted efficiency. More details of the

selected designs can be found in Table II. The efficiency by load point for the selected designs is provided in Fig. 5.

It turns out that U2b, V1, V2, and FH are the better options achieving the weighted efficiency of 93.99%, 94.77%, 95.32%, and 94.41%, respectively, whereas the options U2a and FR with lower slot fills are clearly outperformed. For the better options, load point efficiency as a function of the relative PM content (FH = 0, V1 = 0.65, V2 = 0.91, U2b = 1) are plotted in Fig. 6. As shown in Fig. 6(a), the efficiency of each load point is monotonic with the PM content, except for LP2 and the weighted efficiency, when only three options—FH, V1, and U2b—are compared. The efficiencies of low speed or high torque load points (1, 4, and 6) increase with the PM content; whereas the opposite is true for high speed load points (3 and 5). If V2 is also added into the comparison, as shown in Fig. 6(b), a clear boost in efficiency is observed for load points 3, 5, and 6.

Although U2b has the highest PM content, its weighted efficiency is considerably lower than the other three options with lower PM content or a wound field rotor, all of which feature hairpin windings. This means that on the stator side, hairpin style distributed windings are a better choice for this application than FSCWs. On the rotor side, a rotor with

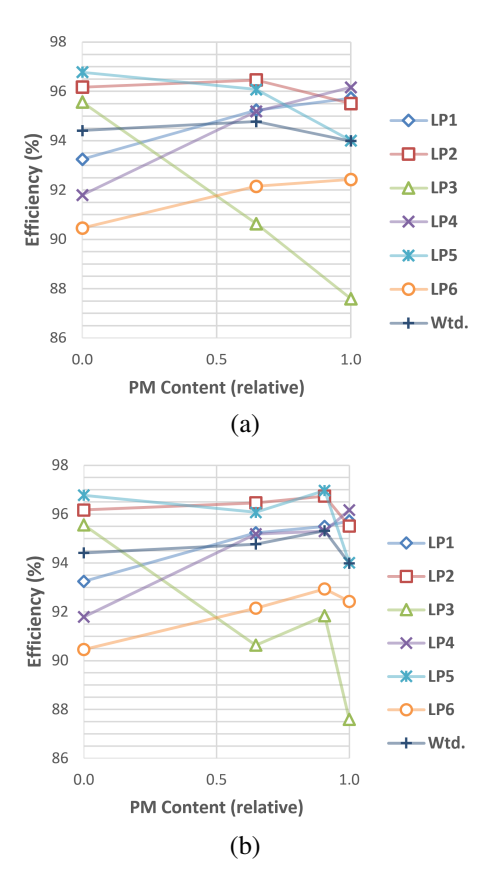


Fig. 6. Comparison of load point and the weighted efficiency of the selected designs, plotted as a function of the relative PM content (FH = 0, V1 = 0.65, V2 = 0.91, U2b = 1), for the better options: (a) FH, V1, and U2b (b) with the addition of V2.

medium or more PM content delivers higher weighted efficiency. Considering the cross-sectional size of this application, an IPM rotor will be confined to either one or two layers, and the V-shape is preferable than the U-shape since it is less complicated with fewer segments and requires lower PM content. However, as a PM-free solution, the efficiency of a wound field rotor with a high slot fill winding is also acceptable, which can have an advantage considering the high cost of rare-earth magnets and the volatility of their market.

Table II also shows that even for the better options, high current densities are inevitable for either the continuous or peak power operation of U.S. DRIVE 2025 targets, forcing the adoption of innovative and aggressive cooling technologies. The weighted efficiency calculated by taking the best load point efficiency from any motor option is 96.13%, which represents the best-case scenario but is most likely unreachable by a single motor option.

VII. OTHER DESIGN CONSIDERATIONS

A. Rotor Mechanical Stress

The maximum operating speed of 20000 rpm imposes a great challenge for the rotor integrity. The mechanical stress is analyzed with 2D FEA at a 20% overspeed, or 24000 rpm, for the IPM rotor of option V2 and the wound field rotor of option

FH. To account for the worst-case scenario, it is assumed that the magnets or the field winding adds only mass or inertia without any contribution to the strength of the rotor structure. For a wound field rotor, the mass of the end turns is also included by multiplying an adjustment factor to the density of the coil side, with the assumption that the end turns are not otherwise supported by any rotor structure.

- 1) IPM Rotors: The samples of option V2 are examined for the rotor mechanical stress. These are two-layer V-shape IPM rotors of which the geometries are generated from 15 parameters. In Fig. 7, the rotor stress distributions of two designs—Design 311 and 392—are provided, with the latter having the lowest value of maximum rotor stress among the samples. It is seen that the stress hotspots are mainly found at two locations that are associated with the bottom magnet layer (Layer 1): the bottom of the center post and the connection between the bridge and the interpolar post. Among the rotor geometry parameters, the pole arc ratio of the bottom layer is found to be very predictive of the maximum rotor stress. As shown in Fig. 7(c), if this number is larger than 0.96, no design can keep the maximum rotor stress below 600 MPa. In other words, the upper bound of the range of this parameter needs to be limited for the rotor to ensure structural integrity. However, the rotor PM content (measured in mm²/pole, since all designs have the same stack length and number of poles) is not a reliable indicator of the maximum rotor stress, as shown in Fig. 7(d). With the same PM content, the maximum rotor stress can vary significantly depending on the placement of magnets. Also, the increase of the maximum rotor stress with the PM content is not clearly noticeable for PM content of 80 mm²/pole or lower, and rather slow above this number. Nonetheless, even with Design 392, which has the lowest value of 478.6 MPa for the maximum rotor stress, further structural optimization may still be needed to alleviate the stress hotspots when rotor lamination materials of comparable yield strengths are not readily available, or the magnetic properties are not satisfactory of such high strength electrical steel grades.
- 2) Wound Field Rotors: A wound field rotor of 0.72 slot fill from option FH is checked for the maximum rotor stress with three different slot designs. In Fig. 8, only the slot bottom angle (between pole neck and slot bottom) is varied, and the maximum rotor stress is 363.3, 373.4, and 378.0 MPa, respectively, for the slot bottom angles of 90°, 108°, and 120°. If necessary, the fillet radii can also be modified independently for three corners —the corner between pole tip and neck, the corner between pole neck and slot bottom, and the corner at the interpolar position of the slot bottom. Compared with the two-layer V-shape IPM rotor of option V2, the wound field rotor stress is considerably lower and much more manageable.

B. Demagnetization Check of PM Rotors

The high power density nature of this application means that the motor is more likely to experience high current densities combined with high temperatures, both of which contribute to the demagnetization threats of a PM rotor. To make sure the designs can withstand the eletromagnetic and thermal

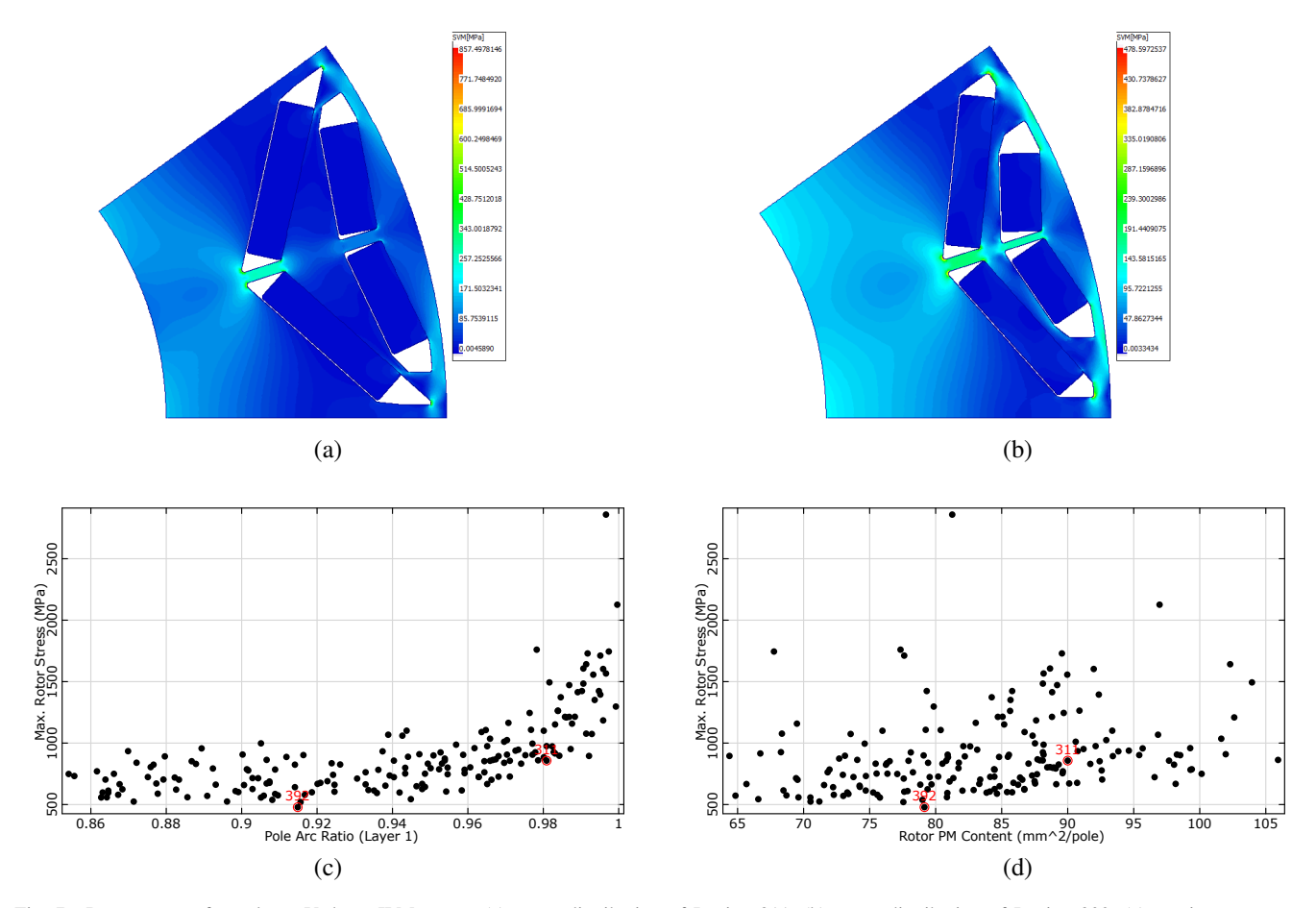


Fig. 7. Rotor stress of two-layer V-shape IPM rotors: (a) stress distribution of Design 311, (b) stress distribution of Design 392, (c) maximum stress as a function of the pole arc ratio of Layer 1, and (d) maximum stress as a function of the PM content.

demagnetization effects, 2D FEA simulations are performed to check the average output torque before and after a worst-case scenario demagnetization currents [14]. It is assumed that the motor is under normal operation at one of the load points when suddenly, "faulty" three-phase demagnetizing currents are applied with a larger magnitude in the negative d-axis for some duration, followed by another period of normal operation. The magnitude of the faulty currents is determined from the maximum instantaneous value of the transient currents following a sudden three-phase short circuit fault, as predicted by the motor's dq model. This demagnetization check is performed at different temperatures for each load point.

For example, the three-phase currents applied to the selected design of option V2 at LP6 with an assumed temperature of 120 °C for the magnets are shown in Fig. 9(a). The faulty currents are about 2.52 times the magnitude of normal operating currents, completely in the negative *d*-axis, and last for one electrical period. The normal operating currents last for two electrical periods prior to and after the demagnetizing currents. As shown in Fig. 9(b), the average torque during the "fault" is virtually zero and after the fault, the average torque output suffers an irreversible loss. To quantify this loss, the ratio of the average torque after and prior to the demagnetization is found to be 0.9649, which means a 3.5%

loss of the torque capability.

For the same design, torque ratios after demagnetization at three different magnet temperatures-100, 120, and 140 °C—are reported for LP1 and LP6 in Fig. 10, which turn out to be the load points most prone to irreversible loss of torque capability with this demagnetization scenario. The magnets are SH grade of which the maximum working temperature (T_{max}) is 150 °C. It is seen that at 100 °C, the loss is almost negligible for both LP1 and LP6. At 120 °C, the loss is 1.5% for LP1 and 3.5% for LP6. However, at 140 °C, or $T_{max} - 10$ °C, losses are about 22% and 25% for the load points. This verifies that the two-layer V-shape IPM rotor design can successfully withstand combined temperature and eletromagnetic demagnetization effects at temperatures around $T_{max}-50$ °C and remain a very reasonable performance up to $T_{max}-30$ °C. Thus the thermal management needs to ensure that the rotor magnets do not exceed $T_{max} - 30$ °C in temperature. Based on this estimation, magnets of higher temperature grades, e.g., UH and EH, are more favorable for this application.

C. Discrete Rectangular Conductor Sizes

For hairpin style windings, rectangular conductors are used instead of conventional round magnet wires. Compared to

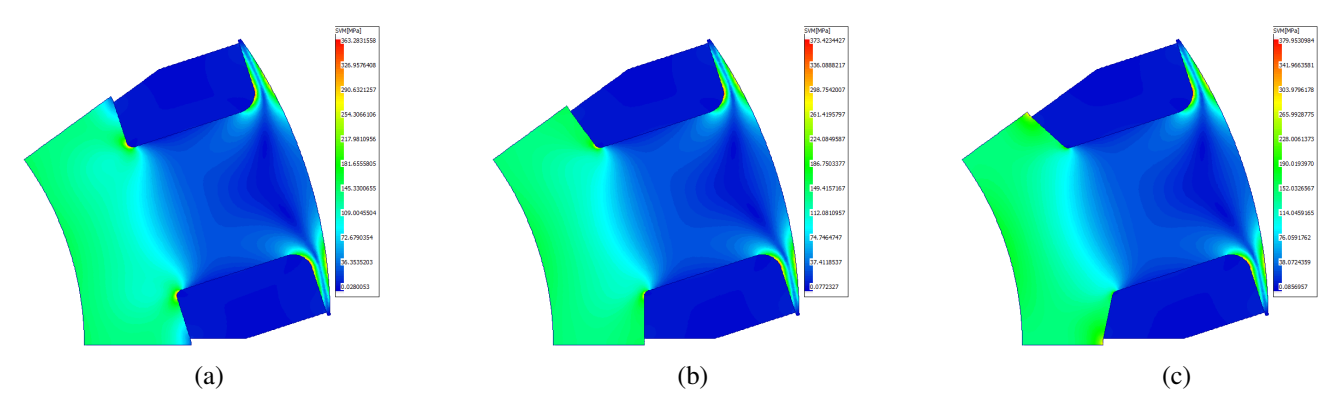


Fig. 8. Comparison of a wound field rotor stress at different slot bottom angles: (a) 90°, (b) 108°, and (c) 120°.

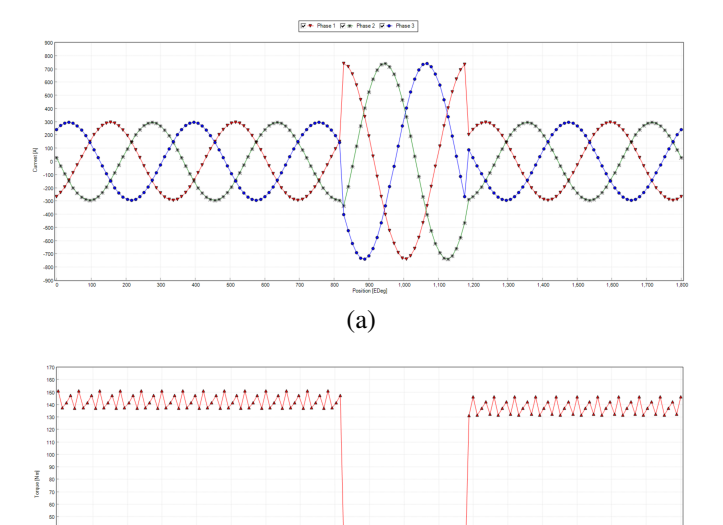


Fig. 9. Demagnetization check of the selected design of option V2 at LP6 and 120 $^{\circ}$ C magnet temperature: (a) currents applied and (b) output torque.

(b)

windings that are wound with round wires, which tend to have a larger number of conductors per slot, hairpin windings typically only have 4, 6, or 8 conductors per slot. Usually dimensional parameters in an electric machine optimization are continuous variables, which means that the conductor size of a hairpin winding resulting from an optimization most likely needs to be custom made. While this is not an issue for mass production in industrial settings, it is a major difficulty for prototyping when it is not possible to order a large amount of a custom size rectangular wire.

To this end, an additional module is developed to automatically select wire from a table of available conductor sizes according to the stator outer diameter, the split ratio (the ratio of rotor outer diameter to stator outer diameter), the airgap length, and the number of conductors per slot. The stator slot is then generated from the selected conductor dimensions rather than directly from the slot width and slot depth parameters. In

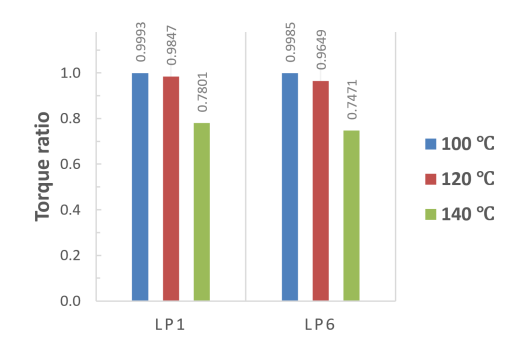


Fig. 10. Torque ratios after demagnetization of the selected design of option V2 for LP1 and LP6 at different temperatures.

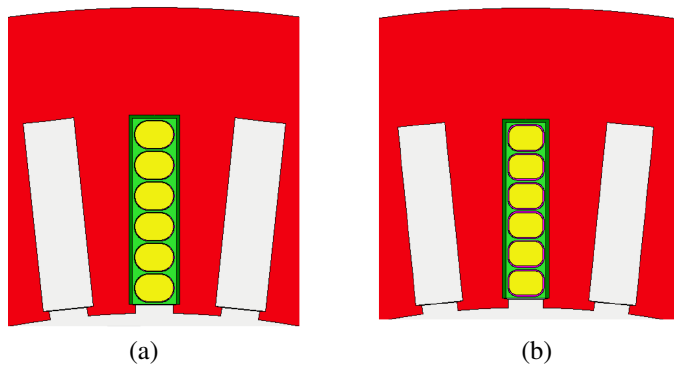


Fig. 11. Resulting geometry after the automatic selection of hairpin winding conductor from available sizes for a split ratio of: (a) 0.72 and (b) 0.73.

Fig. 11, it is shown that different conductor sizes are selected for two designs of different split ratio. For the design with a split ratio of 0.72, a wire of $1.4478 \times 2.0574 \times 0.7239$ mm (bare copper height, width, and corner radius) is selected; whereas for a split ratio of 0.73, a wire of a slightly smaller cross-section, $1.27 \times 1.8288 \times 0.4572$ mm, is selected. The stator laminations generated for these conductors are also shown in Fig. 11.

VIII. CONCLUSION

Six traction motor options are compared for their potential to achieve the U.S. DRIVE 2025 targets. To maximize the

weighted efficiency, a hairpin style distributed winding is strongly preferred on the stator side. On the rotor side, an IPM rotor with medium to high PM content and a wound field rotor with high slot fill windings are both feasible options. IPM rotors have clearly better efficiencies with demagnetization proved not to be a concern, but the mechanical stress at high speeds is more challenging to deal with than a wound field rotor. As a PM-free solution, a would field rotor has the additional advantage in terms of the cost and availability of materials. With any motor option, to reach the continuous and peak power outputs, the current densities will be at levels that force the adoption of extremely aggressive cooling technologies.

Based on this work, the designs of two prototype motors are being finalized. Both motors feature hairpin windings on the stator side and the conductors will be selected from sizes that are carried by wire suppliers. One of them has a two-layer V-shape IPM rotor, and the other has a wound field rotor with an expected high slot fill of 0.72.

REFERENCES

- U.S. DRIVE, "Electrical and electronics technical team roadmap," 2017. [Online]. Available: https://www.energy.gov/sites/prod/files/2017/ 11/f39/EETT%20Roadmap%2010-27-17.pdf
- [2] F. Momen, K. Rahman, and Y. Son, "Electrical propulsion system design of Chevrolet Bolt battery electric vehicle," *IEEE Trans. Ind. Appl.*, vol. 55, no. 1, pp. 376–384, Jan./Feb. 2019.
- [3] M. Salameh, T. Spillman, M. Krishnamurthy, I. P. Brown, and D. C. Ludois, "Wound field synchronous machine with segmented rotor laminations and die compressed field winding," in *Proc. IEEE Energy*

- Convers. Congr. Expo. (ECCE), Baltimore, MD, USA, Sep. 2019, pp. 1739–1746.
- [4] M. Gröninger, F. Horch, A. Kock, M. Jakob, and B. Ponick, "Cast coils for electrical machines and their application in automotive and industrial drive systems," in *Proc. 4th Int. Electr. Drives Prod. Conf. (EDPC)*, Nuremberg, Germany, Sep. 2014, pp. 1–7.
- [5] T. M. Jahns and B. Sarlioglu, Proposed Consensus Interpretation of Machine Requirements for DOE CAEDT Project (Rev. 1), University of Wisconsin-Madison, Mar. 2020, internal communication.
- [6] Six Operating Points Illustration, Purdue University, Jun. 2020, internal communication.
- [7] N. Tang and I. P. Brown, "Family phenomenon in electric machine winding MMF space harmonics: Attribution and applications," *IEEE Trans. Magn.*, vol. 55, no. 5, May 2019, Art. no. 8101310.
- [8] N. Tang and I. P. Brown, "Framework and solution techniques for suppressing electric machine winding MMF space harmonics by varying slot distribution and coil turns," *IEEE Trans. Magn.*, vol. 54, no. 5, May 2018, Art. no. 8103512.
- [9] L. Zhu, S. Z. Jiang, Z. Q. Zhu, and C. C. Chan, "Analytical modeling of open-circuit air-gap field distributions in multisegment and multilayer interior permanent-magnet machines," *IEEE Trans. Magn.*, vol. 45, no. 8, pp. 3121–3130, Aug. 2009.
- [10] A. M. EL-Refaie, "Fractional-slot concentrated-windings synchronous permanent magnet machines: Opportunities and challenges," *IEEE Trans. Ind. Electron.*, vol. 57, no. 1, pp. 107–121, Jan. 2010.
- [11] T. Most and J. Will. (2008) Metamodel of Optimal Prognosis—an automatic approach for variable reduction and optimal metamodel selection. [Online]. Available: https://www.dynardo.de/en/library
- [12] Multiphysics Optimization of Electric Machines with Motor-CAD and optiSLang Software Tools: Application to an IPM Traction Motor, Motor Design Ltd., Wrexham, UK, 2020.
- [13] D. B. Pinhal and D. Gerling, "Performance map calculation of a salient-pole synchronous motor with hairpin winding," in *Proc. IEEE 28th Int. Symp. Ind. Electron. (ISIE)*, Vancouver, BC, Canada, Jun. 2019, pp. 359–365.
- [14] Evaluating Demagnetization Using Motor-CAD, Motor Design Ltd., Wrexham, UK, 2020.